Supporting Information for

Gd-Dots with Strong Ligand–Water Interaction for Ultrasensitive Magnetic Resonance Renography

Xiao-Yu Zheng,[a] Kai Zhao,[b] Jinglong Tang,[c] Xin-Yu Wang,[a] Lin-Dong Li,[a] Nai-Xiu Chen,[a] Yan-Jie Wang,[a] Shuo Shi,[a] Xiaodong Zhang,[b] Sivakumar Malaisamy,[a] Ling-Dong Sun,*[a] Xiaoying Wang,*[b] Chunying Chen,[c] and Chun-Hua Yan*[a]

[a] Beijing National Laboratory for Molecular Sciences, State Key Laboratory of Rare Earth Materials Chemistry and Applications, PKU-HKU Joint Laboratory in Rare Earth Materials and Bioinorganic Chemistry, College of Chemistry and Molecular Engineering, Peking University, Beijing 100871, China
[b] Department of Radiology, Peking University First Hospital, Beijing 100034, China
[c] CAS Key Laboratory for Biomedical Effects of Nanomaterials and Nanosafety & CAS Center for Excellence in Nanoscience, National Center for Nanoscience and Technology of China, Beijing 100190, China

Theoretical Calculation

All calculations were performed with the Gaussian 09 program,[S1] including geometry optimization and single point energies. All gas phase stationary points were optimized using B3LYP[S2,S3] functional and 6-31++G(d,p) basis set[S4] for the monomers and the complexes. All of the energies discussed in the paper and the Supporting Information are the electronic energy with Zero Point vibration Energy (ZPE). Gas phase enthalpies at 298 K (ΔH_{gas}) are also provided for reference.

To compare the binding capacity with water molecules of different polymers (PEG, PEI, PAA) and simplify the computational process, methoxyethane was used as the monomer of PEG, ethylamine/diethylamine/trimethylamine were used as the monomers to PEI, and propanoic acid/propionate ion as the monomers of PAA. Here the interaction energies of the monomers and the water molecules were determined and corrected by the Basis Sets Superposition Error (BSSE) *via* standard counterpoise method.[S5] The energy of binding monomers to water molecules (BE_{mono}) is determined by:

Binding Energy (BE_{mono}) = E(complex)-E(monomer)-E(water),

where BE_{cor} is the corrected binding energy while considering BSSE energy.

	BE(kcal/mol)	E_{BSSE}(kcal/mol)	BE_{cor}(kcal/mol)	ΔH_{gas}(kcal/mol)
Methoxyethane	-8.74	0.64	-8.10	-2.99
Ethylamine	-9.64	0.87	-8.77	-4.54
Diethylamine	-11.11	0.91	-10.20	-4.35
Trimethylamine	-11.58	0.92	-10.66	-3.23
Propanoic acid	-12.83	0.85	-11.98	-7.22
Propionate ion	-21.29	0.78	-20.51	-15.80

The oligomers were also taken into consideration. Trimer or tetramer with three water molecules bonded were calculated using the same method. The interaction energies were also corrected by the Basis Sets Superposition Error (BSSE).

The energy of binding monomers to water molecules (BE_{olig}) is determined by:

BE_{olig} = (E(complex)-E(oligomer)-NE(water))/N,

$BE_{cor,olig}$ = (E(complex)-E(oligomer)-NE(water)+BSSE)/N,

where N is the number of water molecule bonded to the trimer or tetramer. Here lists one of the rational optimized complexation geometries and their binding energies. As shown below, the energies are in accordance with the energies of monomers.

	BE(kcal/mol)	E_{BSSE}(kcal/mol)	BE_{cor}(kcal/mol)
PEG	-4.18	2.15	-3.46
PEI	-6.08	3.01	-5.07
PAA (Propanoic acid)	-9.19	2.85	-8.24
PAA(Propionate ion)	-24.75	2.98	-23.76

Supplementary Figures and Tables

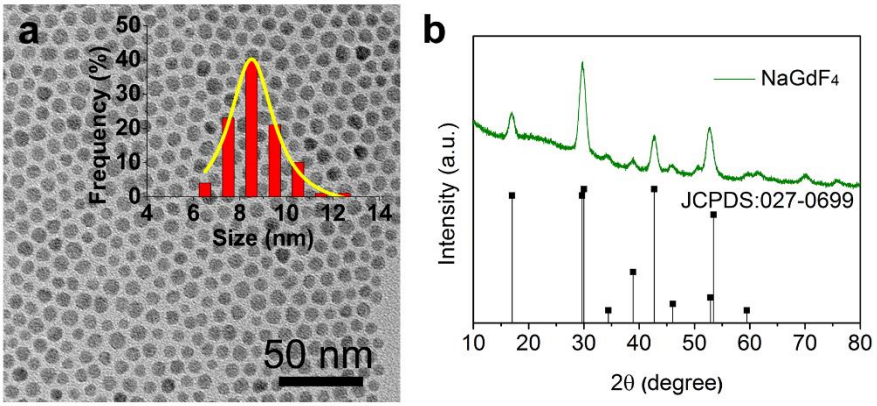

Figure S1. Characterization of 8.6 nm $NaGdF_4$ NPs. a) TEM image and size distribution (inset, with a mean size of 8.6±1.1 nm). b), XRD pattern, revealing the hexagonal phase of $NaGdF_4$ NPs.

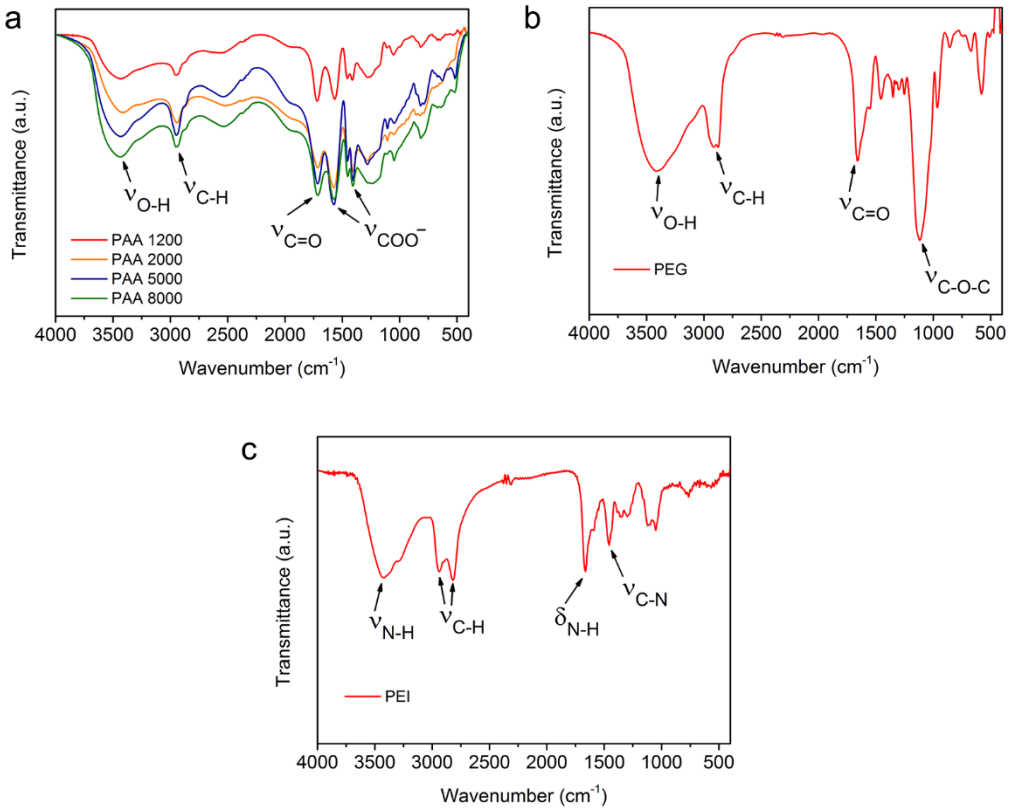

Figure S2. FT–IR spectra of $NaGdF_4$ NPs capped with different polymers, including a) PAA, b) PEG, and c) PEI. PAA with different molecular weights show very similar spectra with characteristic peaks corresponding to carboxyl groups (1715 cm^{-1} and 3435 cm^{-1} for C=O and O–H stretching vibrations, respectively), carboxylate anions (1410 cm^{-1} and 1575 cm^{-1} for COO^- symmetric and asymmetric stretching vibrations, respectively), and methylene groups (2945 cm^{-1} for C–H stretching vibration). Alendronate-modified PEG molecule shows a strong peak at 1117 cm^{-1} corresponding to C–O–C stretching vibration of PEG chain and another peak at 1660 cm^{-1} corresponding to C=O stretching vibration of amide groups. PEI shows characteristic peaks at 1662 cm^{-1} and 1458 cm^{-1} corresponding to N–H deformation vibration and C–N stretching vibration, respectively. These results confirm the presence of different polymers on the surface of $NaGdF_4$ NPs.

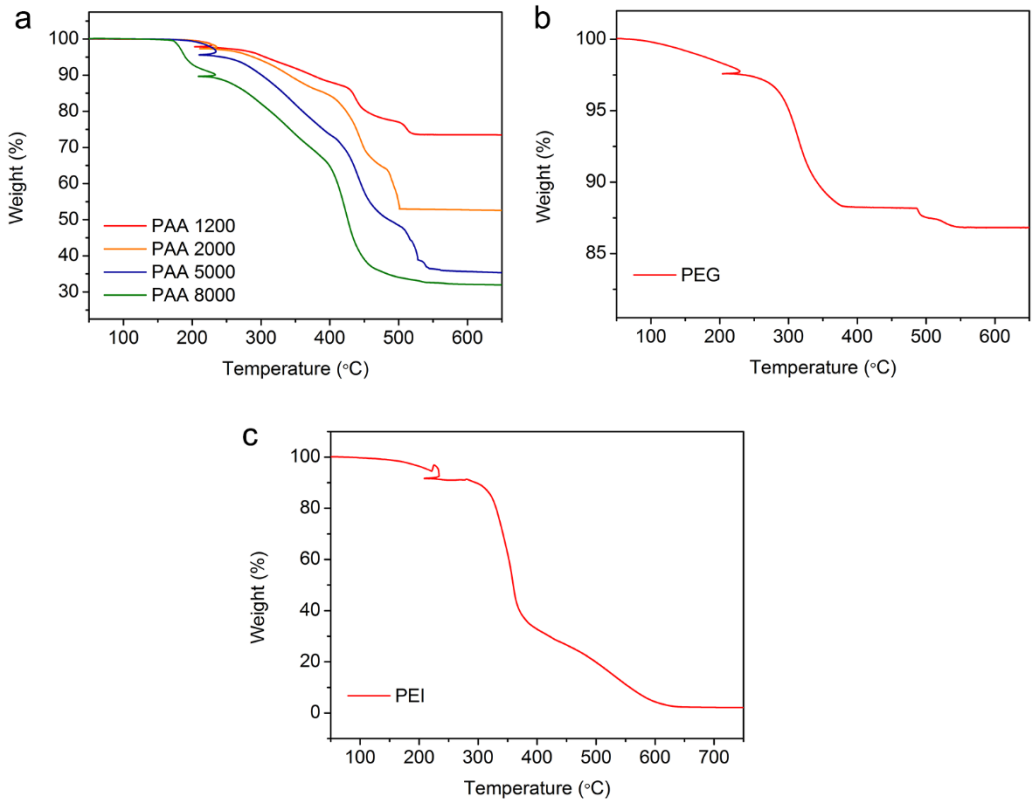

Figure S3. TGA curves of $NaGdF_4$ NPs capped with different polymers, including a) PAA, b) PEG, and c) PEI. The amount (by weight) of PAA on $NaGdF_4$ NPs was measured to be 26.5% for PAA_{1200}, 47.4% for PAA_{2000}, 64.4% for PAA_{5000}, and 68.0% for PAA_{8000}. For PAA, the ligand amount increases monotonously with molecular weight increasing, which is consistent with the increasing hydrodynamic size in water. By contrast, PEG-capped NPs with a small hydrodynamic size show the least weight loss of 13.2% among these NPs, while PEI-capped ones with the second largest hydrodynamic size show the most weight loss of up to 97.6%. Therefore, the ligand amount relies on both molecular weight and the characteristics of polymers.

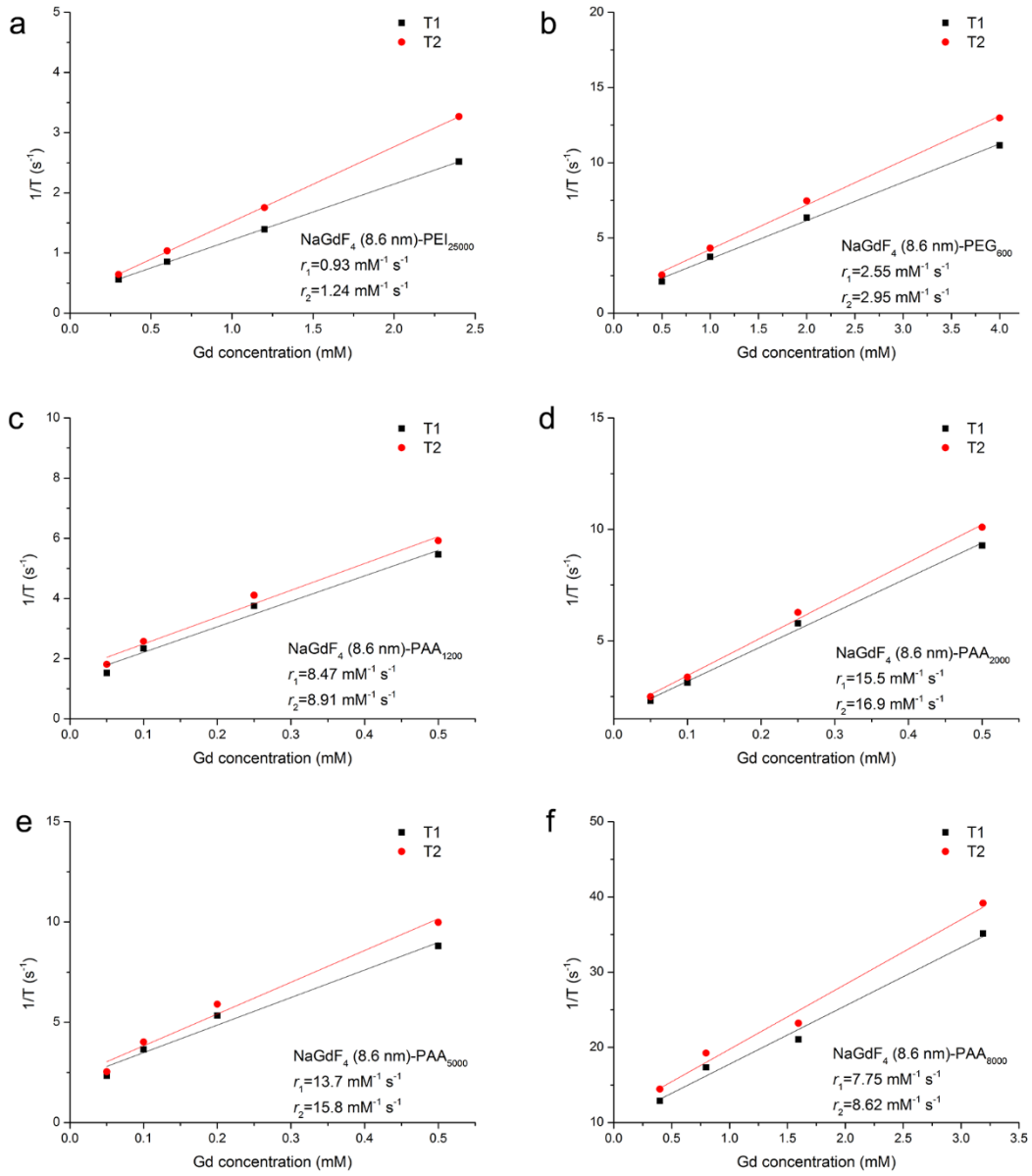

Figure S4. Plots of T_1 and T_2 relaxation times *versus* their Gd^{3+} concentration for 8.6 nm-sized $NaGdF_4$ capped with different surface ligands at 0.5 T, including a) PEI_{25000}, b) alendronate-modified PEG_{600}, c) PAA_{1200}, d) PAA_{2000}, e) PAA_{5000}, and f) PAA_{8000}.

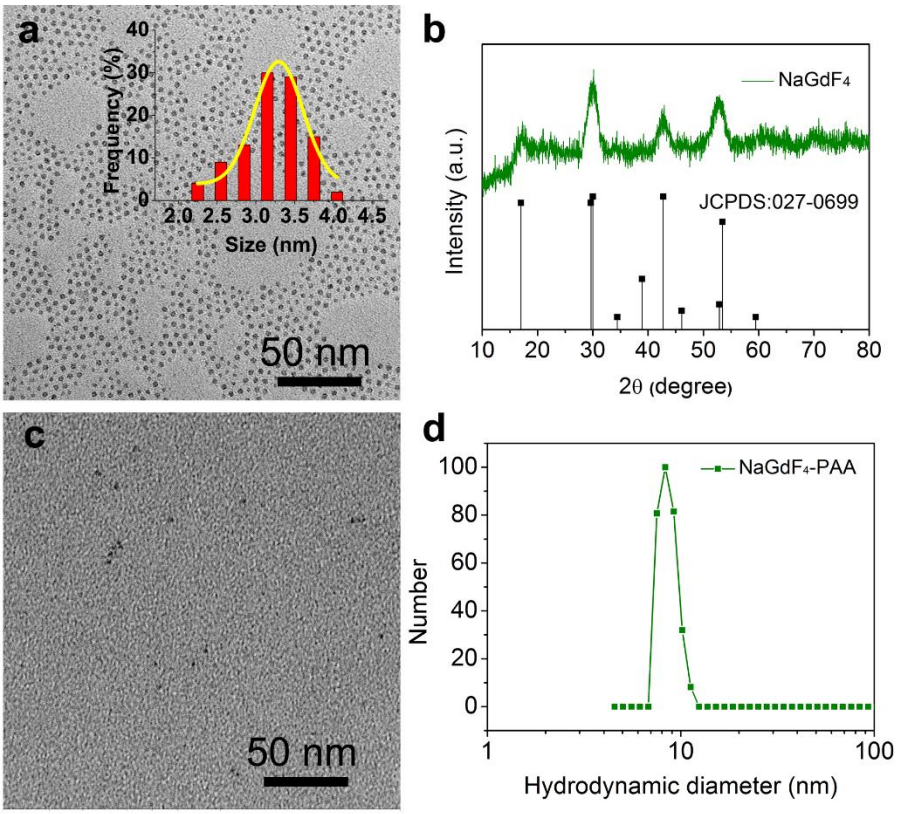

Figure S5. a) TEM image of OA-capped $NaGdF_4$ NPs (inset: size distribution with a mean size of 3.2±0.4 nm). b) XRD pattern of OA-capped $NaGdF_4$ NPs, revealing the hexagonal structure of $NaGdF_4$ NPs. c) TEM image of PAA_{2000}-capped $NaGdF_4$ NPs. d) hydrodynamic size distribution of PAA_{2000}-capped $NaGdF_4$ NPs.

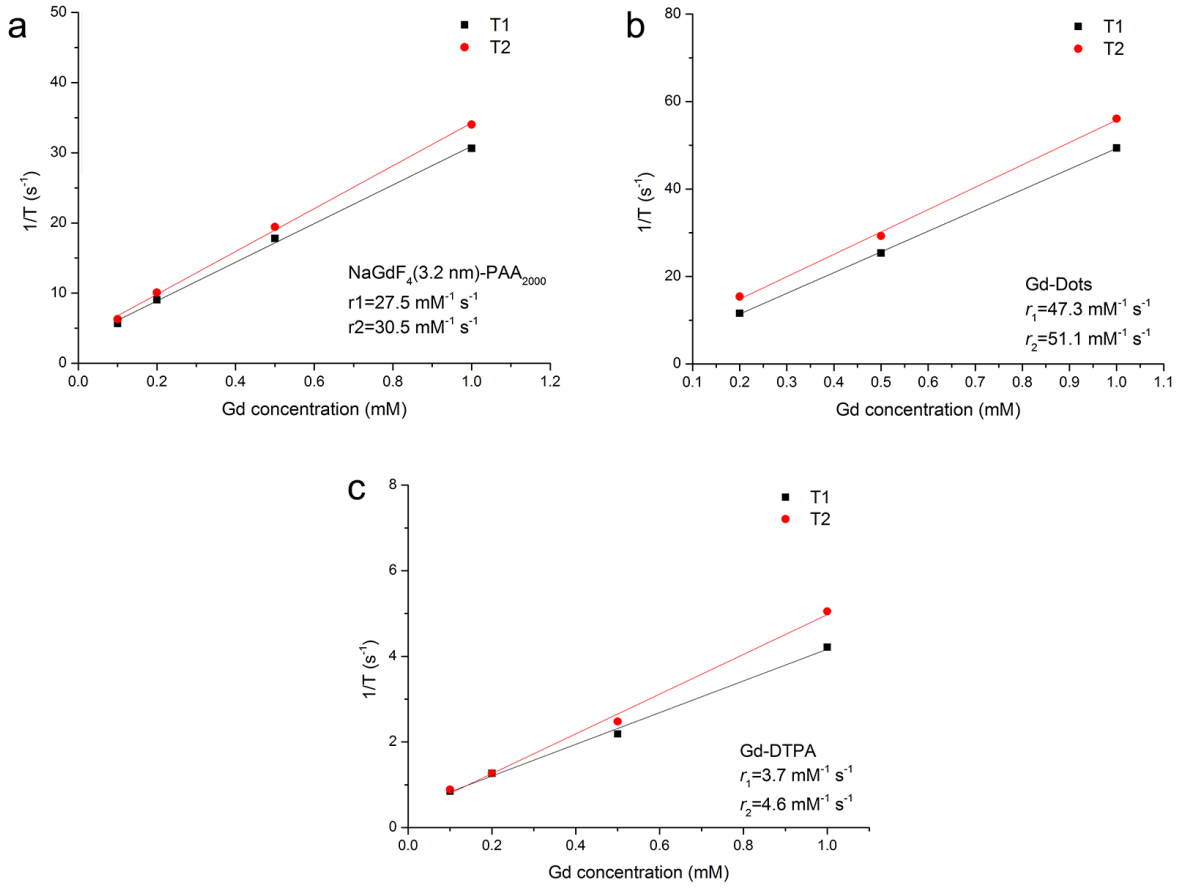

Figure S6. Plots of T_1 and T_2 relaxation times *versus* their Gd^{3+} concentration for a) 3.2 nm $NaGdF_4$ NPs, b) Gd-dots, and c) Gd-DTPA at 0.5 T.

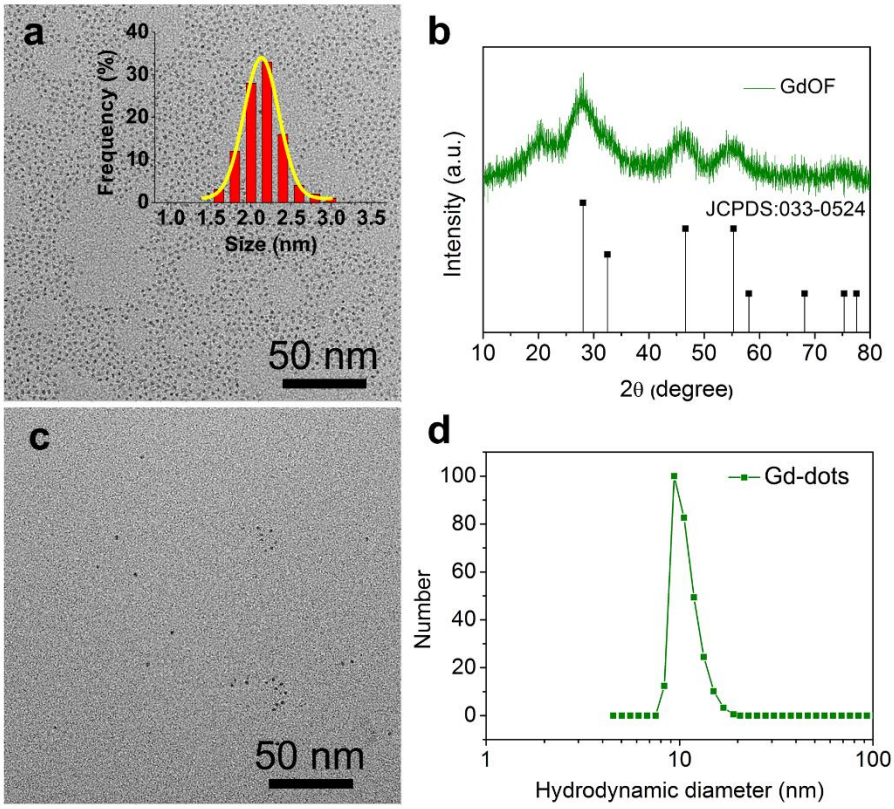

Figure S7. a) TEM image of OA-capped GdOF NPs (inset: size distribution with a mean size of 2.1±0.2 nm). b) XRD pattern of OA-capped GdOF NPs, revealing the cubic phased structure of GdOF NPs. c) TEM image of Gd-dots. d) hydrodynamic size distribution of Gd-dots.

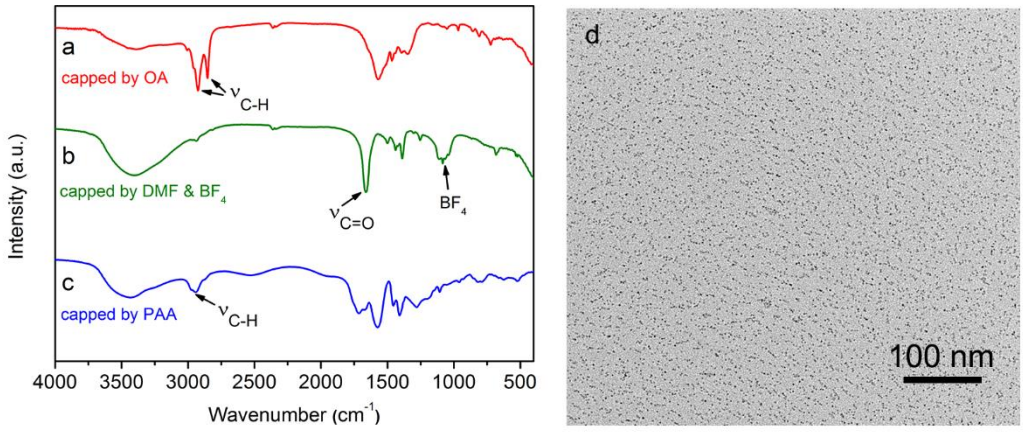

Figure S8. FT–IR spectra of GdOF NPs in different stage of ligand-exchange process. a) capped by OA before $(CH_3)_3OBF_4$ treatment; b) capped by BF_4^- and solvent DMF molecules; c) capped by PAA. After $(CH_3)_3OBF_4$ treatment, the intensity of the characteristic C–H stretching vibrations at 2800–3000 cm^{-1} is greatly reduced, indicating the removal of OA molecules. Meanwhile, new peaks at 1084 and 1664 cm^{-1} can be assigned to BF_4^- anions and solvent DMF molecules, respectively, implying that the particle surface is capped by BF_4^- and DMF. After PAA capping, the intensity of C–H stretching vibrations at 2800–3000 cm^{-1} recovers and the characteristic peaks of BF_4^- anions disappears, suggesting the existence of PAA on particle surface. d) TEM image of GdOF NPs after $(CH_3)_3OBF_4$ treatment. No obvious agglomeration can be observed, indicating the good dispersibility of NPs.

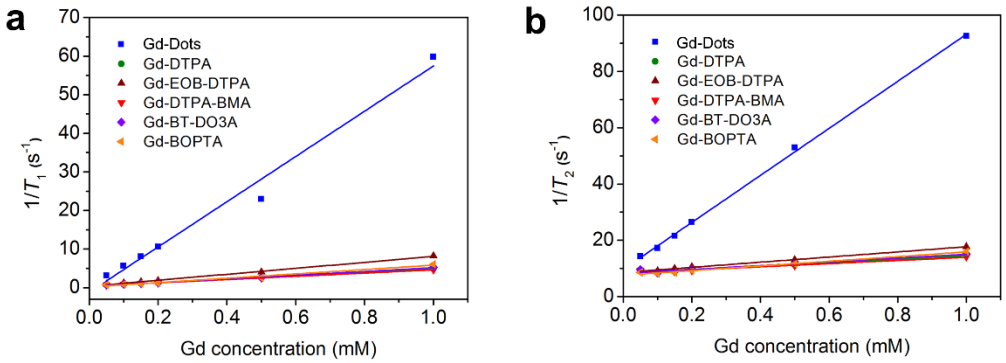

c

	r_1 (mM^{-1} s^{-1})	r_2 (mM^{-1} s^{-1})	r_2/r_1
Gd-Dots	58.6 ± 3.7	83.5 ± 1.2	1.4
Gd-DTPA	4.4 ± 0.1	6.1 ± 0.5	1.4
Gd-EOB-DTPA	7.7 ± 0.2	9.1 ± 0.3	1.2
Gd-DTPA-BMA	4.2 ± 0.1	5.6 ± 0.6	1.3
Gd-BT-DO3A	4.8 ± 0.2	6.7 ± 0.8	1.4
Gd-BOPTA	5.6 ± 0.4	8.3 ± 0.4	1.5

Figure S9. Plots of a) T_1 and b) T_2 relaxation times *versus* their Gd^{3+} concentrations for Gd-dots and five clinically approved MRI CAs at 3 T. c) Summary of relaxivities (r_1 and r_2) and r_2/r_1 values for CAs.

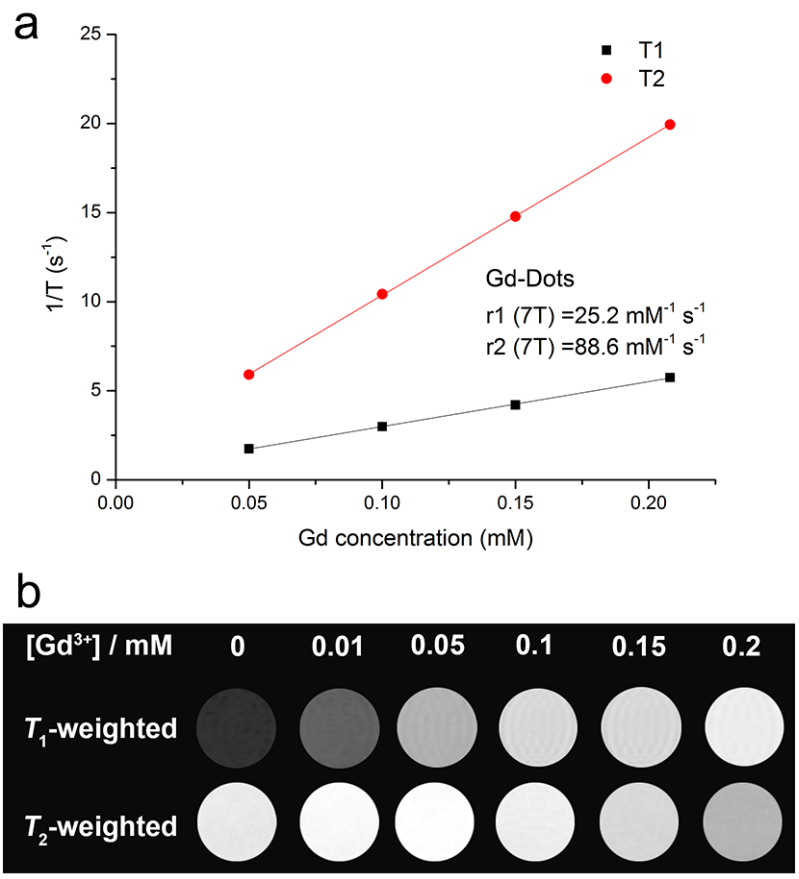

Figure S10. a) Plots of T_1 and T_2 relaxation times *versus* their Gd^{3+} concentration for Gd-dots and b) T_1- and T_2-weighted MR images at 7 T.

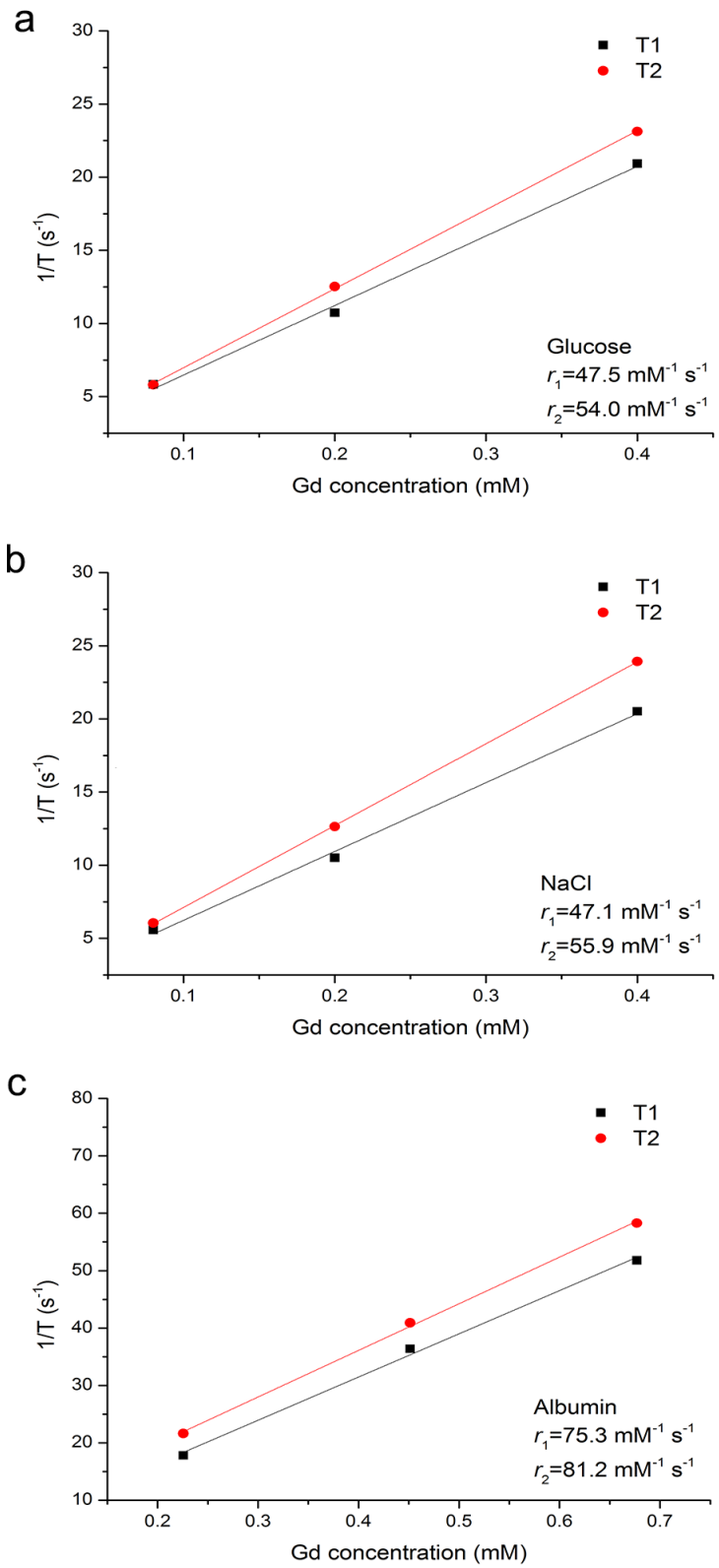

Figure S11. Plots of T_1 and T_2 relaxation times *versus* their Gd^{3+} concentration for Gd-dots in different dispersion media at 0.5 T, including a) 5% glucose solution, b) 0.9% NaCl solution, and c) bovine serum albumin dispersion (50 mg/mL).

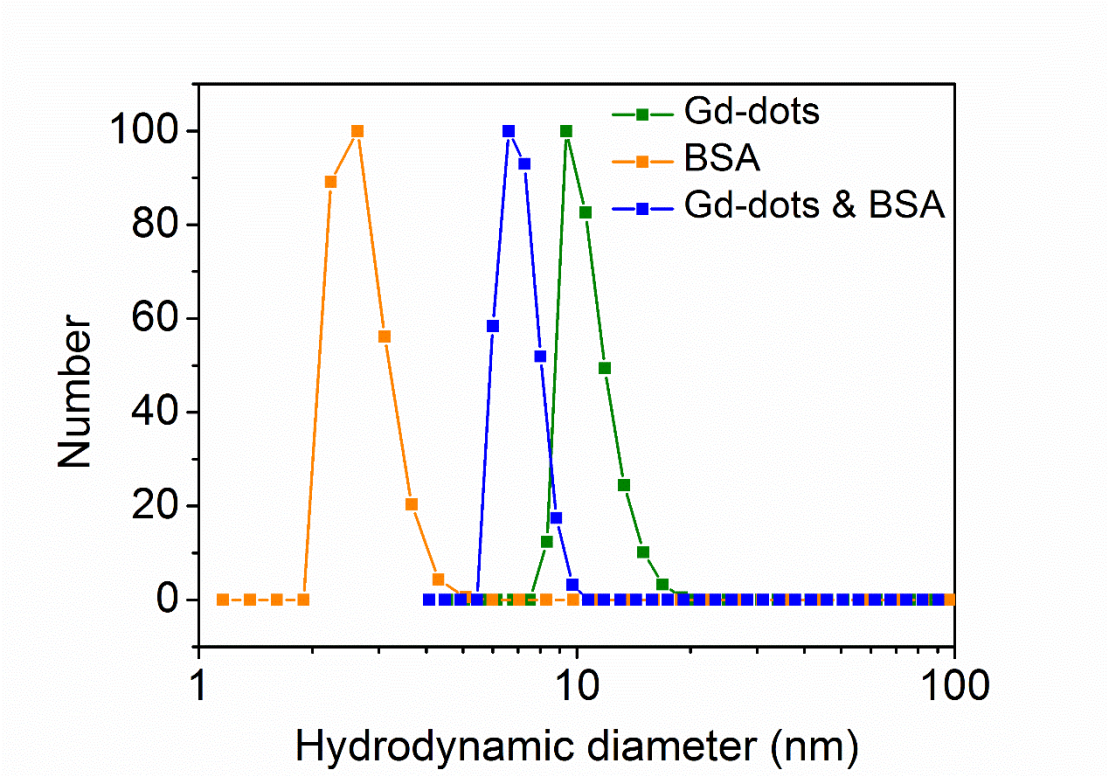

Figure S12. Hydrodynamic size distribution of Gd-dots, BSA dispersion (50 mg/mL), and the mixed solution. After mixing with BSA dispersion, the hydrodynamic size of Gd-dots does not increase but decreases, implying no obvious adsorption between Gd-dots and BSA particles. The phenomenon can be attributed to the electrostatic repulsion between them as both of them are negatively charged in pure water.

Table S1. Summary of experimental proton relaxation times and calculated MR signal intensity for all six CAs. Experimental T_1 and T_2 values were inserted in equation S(TR,TE)=ρe^(-TR/T2) (1-e^(-TR/T1)), which is the theoretical expression for a spin echo sequence.[S6] The T_1- and T_2-weightd sequences applied in this study are spin echo sequences with TR/TE of 600/11 ms and 3000/96 ms, respectively.

	Gd/mM	0.05	0.1	0.15	0.2	0.5	1
T_1/ms	Gd-Dots	318.1876	178.1325	123.3395	94.61633	43.63002	16.71905
	Gd-DTPA	1443.356	1157.354	946.2528	808.2114	393.5304	204.1566
	Gd-EOB-DTPA	1105.803	832.016	658.9352	547.6451	248.3732	121.9869
	Gd-DTPA-BMA	1481.635	1171.111	962.0935	846.9552	406.719	216.0714
	Gd-BT-DO3A	1442.356	1139.536	935.7163	808.3421	389.2565	189.9877
	Gd-BOPTA	1441.421	1151.212	957.6709	830.4958	397.6459	164.8098
T_2/ms	Gd-Dots	69.92029	58.05852	46.37789	37.7672	18.90395	10.80322
	Gd-DTPA	107.6716	114.9161	110.5767	101.8206	88.23789	68.32935
	Gd-EOB-DTPA	107.371	109.8877	100.6958	94.58054	76.27765	56.39204
	Gd-DTPA-BMA	106.2733	115.3017	112.5657	108.2708	91.33254	70.70636
	Gd-BT-DO3A	104.3427	119.8365	112.7536	102.3625	85.01955	66.22078
	Gd-BOPTA	117.3158	123.1239	116.9358	107.087	86.49023	62.46486
Signal intensity (TR/TE= 600/11ms)	Gd-Dots	0.72479	0.798899	0.782762	0.746006	0.558841	0.361239
	Gd-DTPA	0.307089	0.367614	0.425112	0.470359	0.690614	0.806251
	Gd-EOB-DTPA	0.377983	0.46486	0.535848	0.592575	0.788396	0.816769
	Gd-DTPA-BMA	0.300252	0.364425	0.420812	0.458543	0.683756	0.802657
	Gd-BT-DO3A	0.306261	0.373447	0.429352	0.470577	0.690538	0.810951
	Gd-BOPTA	0.310014	0.371471	0.423754	0.464223	0.685828	0.816534
Signal intensity (TR/TE= 3000/96ms)	Gd-Dots	0.253328	0.191378	0.126192	0.078718	0.00623	0.000138
	Gd-DTPA	0.358701	0.401237	0.402094	0.380006	0.336736	0.245377
	Gd-EOB-DTPA	0.381846	0.406097	0.38138	0.360886	0.284061	0.182252
	Gd-DTPA-BMA	0.35172	0.401353	0.407351	0.400098	0.349333	0.257245
	Gd-BT-DO3A	0.348713	0.416573	0.409519	0.381902	0.323162	0.234642
	Gd-BOPTA	0.386133	0.424687	0.420822	0.396997	0.329401	0.215055

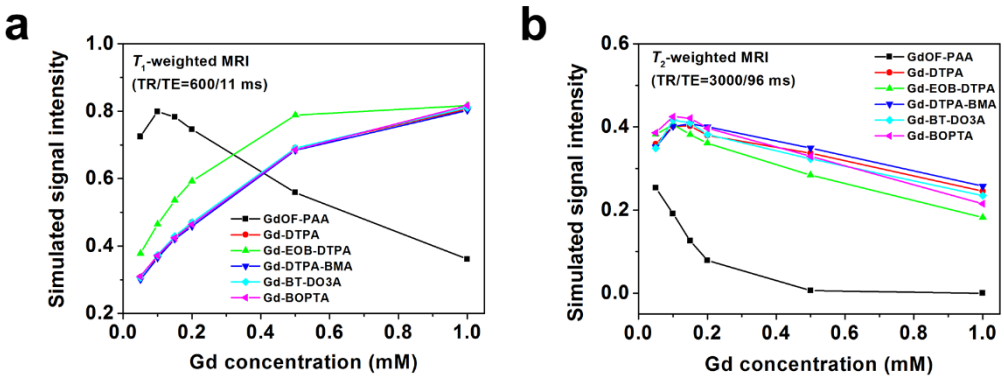

Figure S13. Plots of simulated MR signal intensity *versus* Gd concentration for CAs according to Supplementary Table S1. a) For T_1-weighted MRI (TR/TE = 600/11 ms); b) For T_2-weighted MRI (TR/TE = 3000/96 ms). The simulated MR signal intensity fitted well with the experimental MRI images.

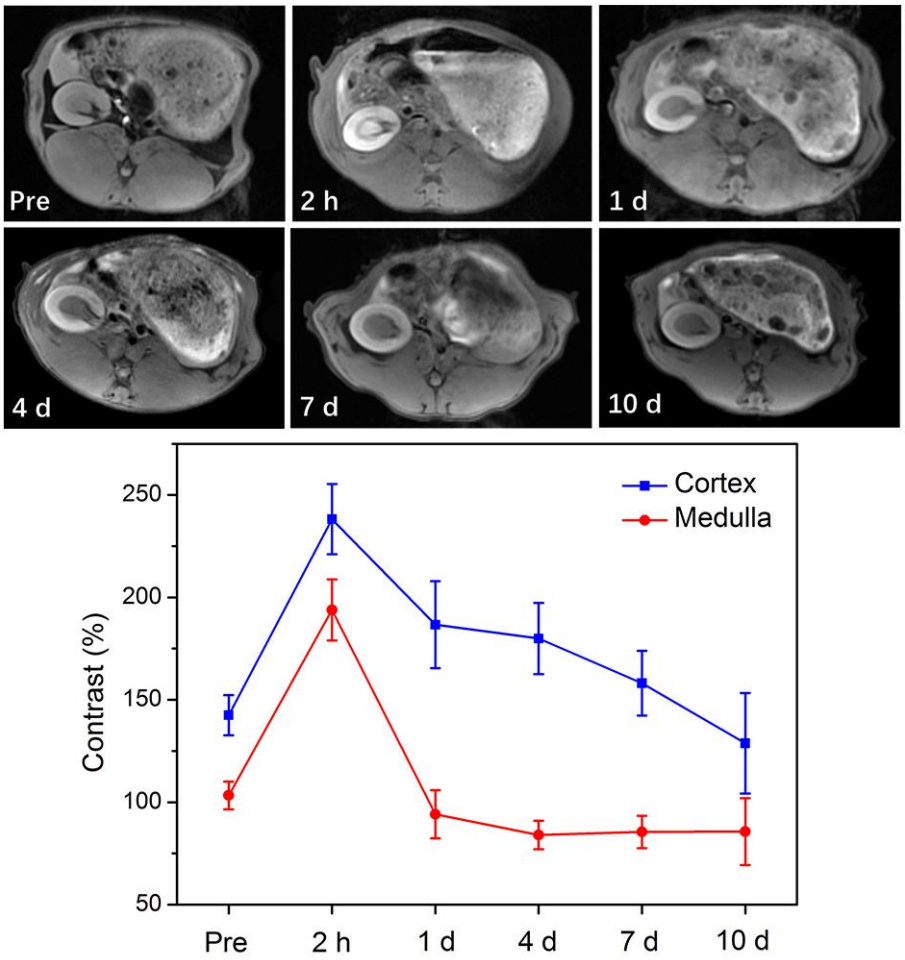

Figure S14. T_1-weighted MRI of kidney at different time points post injection. This process was expressed using the change of contrast (Contrast = Signal intensity of kidney / Signal intensity of adjacent muscular tissue, analyzed by ImageJ software). Both of the contrasts in cortex and medulla regions drastically increased 2 h post injection. The contrast in medulla region recovered to that before injection within 1 day, while the contrast in cortex region gradually decreased in the following 10 days. These results suggest the clearance of Gd-dots from the cortex is slower than that from the medulla.

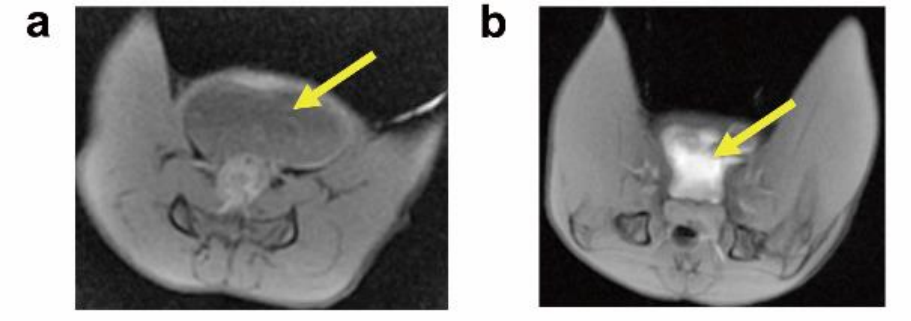

Figure S15. T_1-weighted MRI of urinary bladder: b) before injection; c) 2 h post injection. The urinary bladder is indicated by yellow arrow. The significantly enhanced MR signal intensity of urinary bladder indicated that the Gd-dots were excreted into the urine.

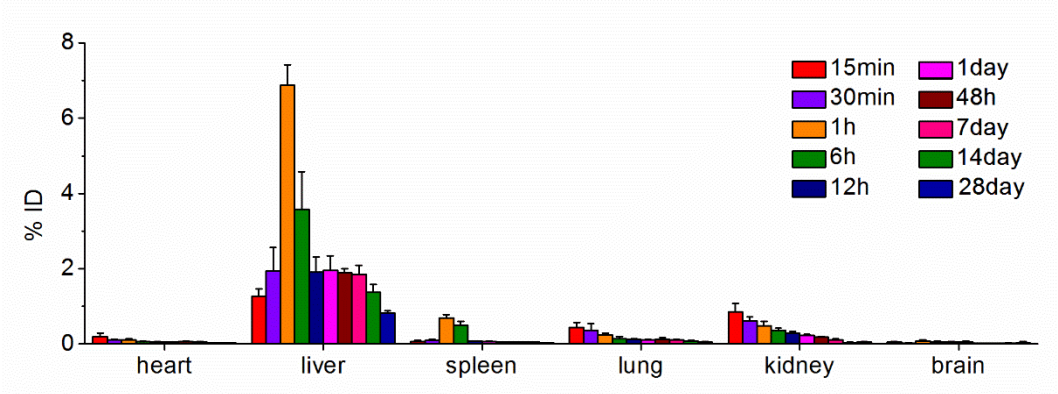

Figure S16. Time-dependent biodistribution of Gd-dots in tissues after intravenous injection with a dose of 0.01 mmol Gd/kg body weight (n = 6). The amount of Gd detected in blood and all organs 12 h post injection is less than 3% ID (0.06% ID in heart, 1.91% ID in liver, 0.08% ID in spleen, 0.13% ID in lung, 0.28% ID in kidney, 0.04% ID in brain, and 0.2% ID in blood).

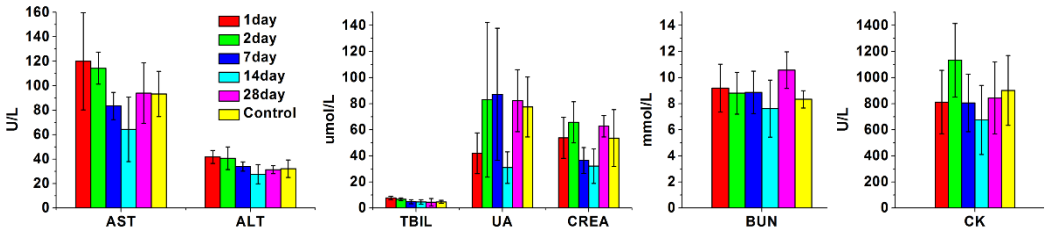

Figure S17. Serum biochemical analysis of mice at different time points after intravenous injection of Gd-dots with a dose of 0.01 mmol Gd/kg body weight (n = 6). The liver function is revealed by alanine aminotransferase (ALT), aspartate aminotransferase (AST), and total bilirubin (TBIL), while creatinine (CREA), uric acid (UA), and blood urea nitrogen (BUN) for kidney function and creatine kinase (CK) for myocardial physiological situation. The biochemistry indexes of treated mice appeared to be normal compared to those in control group.

References

[S1] Gaussian 09, Revision A.1, Frisch, M. J.; Trucks, G. W.; Schlegel, H. B.; Scuseria, G. E.; Robb, M. A.; Cheeseman, J. R. Gaussian Inc., Wallingford CT, **2009**.
[S2] Becke, A. D. J. Density-Functional Thermochemistry. III. The Role of Exact Exchange. *J. Chem. Phys.* **1993**, *98*, 5648–5652.
[S3] Lee, C.; Yang, W.; Parr, R. G. Development of the Colle-Salvetti Correlation-Energy Formula into a Functional of the Electron Density. *Phys. Rev. B.* **1988**, *37*, 785–789.
[S4] Hehre, W. J.; Radom, L.; Schleyer, P. V. R.; Pople, J. A. *Ab Initio Molecular Orbital Theory,* Wiley, New York, **1986**.
[S5] Boys, S. F.; Bernardi, F. The Calculation of Small Molecular Interactions by the Differences of Separate Total Energies. Some Procedures with Reduced Errors. *Mol. Phys.* **1970**, *19*, 553–566.
[S6] Lee, N.; Hyeon, T. Designed Synthesis of Uniformly Sized Iron Oxide Nanoparticles for Efficient Magnetic Resonance Imaging Contrast Agents. *Chem. Soc. Rev.* **2012**, *41*, 2575–2589.

Author Contributions

X.-Y. Zheng, L.-D. Sun and C.-H. Yan conceived the idea and experiments. X.-Y. Zheng carried out the synthesis and performed the characterization. S. Shi and S. Malaisamy assisted in the synthesis. X.-Y. Wang performed the quantum computing calculation. X.-Y. Zheng, K. Zhao, X. Zhang and X. Wang carried out the MRI experiments. Y.-J. Wang performed the cell cytotoxicity analysis. J. Tang, L.-D. Li, N.-X. Chen and C. Chen assisted in the pharmacokinetics, biodistribution, and toxicity studies. X.-Y. Zheng, L.-D. Sun and C.-H. Yan co-wrote the paper. All authors discussed the results and commented on the manuscript.